RESEARCH ARTICLE | JUNE 11 2025

Effect of oxygen vacancy modification on electrical properties of $La(Cr_{0.2}Mn_{0.2}Fe_{0.2}Co_{0.2}Ni_{0.2})O_3$ high-entropy perovskite oxide films

Xin Yuan ; Sheung Mei Ng ; PeiGen Li ; JingMing Liang ; Hon Fai Wong ; ChuangShi Feng ; Shuai Nan ; HongQuan Song ; Zhou Guan ; FuXiang Zhang ; Chi Wah Leung

AIP Advances 15, 065321 (2025)
https://doi.org/10.1063/5.0267185

Effect of oxygen vacancy modification on electrical properties of $La(Cr_{0.2}Mn_{0.2}Fe_{0.2}Co_{0.2}Ni_{0.2})O_3$ high-entropy perovskite oxide films

Cite as: AIP Advances 15, 065321 (2025); doi: 10.1063/5.0267185
Submitted: 16 March 2025 • Accepted: 27 May 2025 •
Published Online: 11 June 2025

Xin Yuan,[1,2] Sheung Mei Ng,[1] PeiGen Li,[1] JingMing Liang,[1] Hon Fai Wong,[1] ChuangShi Feng,[2] Shuai Nan,[2] HongQuan Song,[2] Zhou Guan,[2] FuXiang Zhang,[2] and Chi Wah Leung[1,a)]

AFFILIATIONS

[1] Department of Applied Physics, Hong Kong Polytechnic University, Hung Hom, Hong Kong, China
[2] Songshan Lake Materials Laboratory, Dongguan, Guangdong 523808, China

[a)] **Author to whom correspondence should be addressed:** dennis.leung@polyu.edu.hk

ABSTRACT

The epitaxial $La(Cr_{0.2}Mn_{0.2}Fe_{0.2}Co_{0.2}Ni_{0.2})O_3$ (L5BO3) thin films with varying oxygen vacancies were prepared on (001) $SrTiO_3$ substrates in this work. These thin films exhibit a high degree of crystallinity and prominent semiconductor characteristics. The valence state of the B-site elements is influenced by the introduction of oxygen vacancies, which in turn affects the spin state. Electrical properties were investigated across a broad temperature range (150–400 K), demonstrating significant resistivity variations of up to 3 orders of magnitude as a function of oxygen vacancies. The corresponding mechanisms of small polaron hopping and variable range hopping are discussed. This work explores the effect of oxygen vacancies on the structure and performance of L5BO3 high-entropy oxide films prepared under various oxygen pressures, offering foundational insights into the compositional manipulation of high-entropy oxides.

I. INTRODUCTION

Perovskite oxides of chemical formula ABO_3 (where A and B are the cations with different sizes) exhibit strong electron correlations due to their specific cation compositions, resulting in the unusual magnetic properties of long and balanced carrier diffusion length, high defect tolerance, and readily tunable bandgap. These unique properties arise from the local bonding between A- and B-site cations. In addition, the corner-sharing oxygen octahedral units in perovskites allow for structural control.[1] The structural diversity of ABO_3 offers possibilities to manipulate electronic, catalytic, and magnetic properties through modification techniques such as changing the microstructure, doping elements, and controlling the interfaces.[2–4]

Isovalent cation doping is a common method for altering perovskite properties. This technique induces internal chemical pressure, which can enhance carrier concentration, alter the valence banding states, and modify magnetic ordering.[5–7] However, increasing dopants in a single cation sublattice can destabilize the phase structure due to the higher formation enthalpy from multiple atomic species.[8] This challenge has been addressed by high-entropy oxides (HEOs), which stabilize structures through entropy-driven processes. In HEOs, the entropy provided by multiple elements overcomes formation enthalpy, leading to a single homogeneous structure with randomly distributed cations.

The formation and stabilization of single-phase HEOs can be quantitatively understood through the Gibbs free energy equation,

$$\Delta G = \Delta H - T\Delta S, \quad (1)$$

where ΔG is the Gibbs free energy change, ΔH is the enthalpy of formation, T is the absolute temperature, and ΔS is the entropy change, primarily dominated by the configurational entropy in multicomponent systems. For an ideal solid solution with N equimolar components, the configurational entropy can be expressed as Eq. (2)

$$\Delta S_{\text{config}} = -R\sum_{i=1}^{N} x_i \ln x_i = R \ln N \quad (\text{for equimolar mixtures}), \quad (2)$$

where R is the gas constant and $x_i = 1/N$ is the molar fraction of each component.

In conventional binary or ternary oxides, a positive enthalpy of mixing ($\Delta H > 0$) often leads to phase separation. However, in HEOs composed of five or more cations, the large positive configurational entropy can dominate the Gibbs free energy at sufficiently high temperatures. As a result, the $-T\Delta S$ term becomes significant enough to render $\Delta G < 0$, thereby thermodynamically favoring the formation of a single-phase solid solution despite a positive enthalpy.

This entropy-dominated stabilization mechanism was experimentally demonstrated by Rost *et al.* in their seminal work on (MgCoNiCuZn)O, where a single-phase rock-salt structure was observed to form above a critical temperature due to high configurational entropy and was retained upon cooling.[9] Therefore, the phase stability of HEOs is not merely an outcome of favorable enthalpy but rather a result of entropy-driven thermodynamic stabilization, particularly effective at high temperatures.

Recent advancements in material synthesis[10,11] have enabled the fabrication of high-entropy perovskites—single-phase metal oxides with five or more metal cations at the A or B sites. This discovery has increased configurational complexity in single crystals and introduced novel design methodologies. The unique structural characteristics of HEOs also help to reveal the internal mechanisms of electrical behavior in strongly disordered systems. Oxygen vacancies, in particular, can influence the electrical properties of HEOs; however, their underlying mechanism remains unclear. This research applies similar techniques to perovskite oxides to study the underlying principles. High-entropy perovskites exhibit significant lattice distortion due to the mismatch of atomic sizes and various bonding characters, impacting electronic properties and leading to unique mechanical behaviors such as enhanced hardness and resistance to thermal expansion. The electronic structure in high-entropy perovskites is complex and highly localized due to the presence of multiple atoms. This localization can result in novel electronic behaviors, such as small polaron hopping, variable range hopping, and unique electric properties not found in simple perovskites. Enhanced configurational entropy in these materials increases crystal stability at high temperatures and introduces intriguing mechanical properties.

High-entropy perovskite ceramics represent a promising frontier in materials science, offering opportunities for developing materials with superior performance in demanding applications. The latest entropy-stabilized synthesis methods overcome the limitations of traditional doping, enabling the realization of high uniformity in disordered states and further advancing the development of functional materials. Ongoing research is crucial for understanding the mechanisms underlying their properties and exploiting their potential in various technological applications.

The multi-element synergy in high entropy perovskite induces severe lattice distortion, which promotes the spontaneous formation of oxygen vacancies with rich concentrations. The oxygen vacancy can enhance the electronic conductivity of the material, decrease the charge transfer resistance ($R_{ct} = 0.44\ \Omega$), and facilitate rapid charge transfer at the interface between the electrode and the electrolyte.[12] These vacancies exhibit exceptional thermal stability due to the high-configurational entropy ($\Delta S_{\text{config}} > 1.5$ R), suppressing vacancy clustering even at 1300 °C.[13]

Just like oxygen, sulfur is also a Group-6 element. While sulfur vacancies in high entropy sulphides [e.g., (CuAgZnCoMnInGa)S] are rich, their stability is limited by sulfur volatilization above 600 °C, leading to vacancy coalescence and phase segregation.[14,15] In addition, sulfur vacancies in traditional chalcogenides (e.g., ZnS, MoS_2, and SnS_2) are prone to passivation by ambient oxygen or moisture, severely degrading carrier mobility.[16] High entropy perovsk can regulate oxygen vacancies to endow high-entropy materials with higher thermal stability and better electrical transport properties.

In 2020, Sharma successfully fabricated $La(Cr_{0.2}Mn_{0.2}Fe_{0.2}Co_{0.2}Ni_{0.2})O_3$(L5BO3) thin films on (001) $SrTiO_3$ substrates, which exhibited strong magnetic anisotropy. The magnetic properties could be manipulated by adjusting lattice symmetry.[17] Brahlek compared the structure of L5BO3 between theoretical calculations and experimental results, finding a relatively homogeneous orthorhombic structure with weak disorder, contrary to the theoretical average of all doped materials. The principle determining L5BO3's structure remains unclear.[18] In 2023, Mohana investigated the electrocatalytic properties of L5BO3 for water oxidation. The B-site cations exhibit a wide range of binding energies, which benefits oxygen evolution reaction (OER) activity. Changes in the valence of surface B-site elements suggest a cooperative effect during OER processing, potentially enhancing OER activity.[19]

While these studies have provided important insights into the structure, magnetism, and catalytic activity of L5BO3, they primarily focus on intrinsic electronic or compositional features without deliberate control over oxygen stoichiometry. Oxygen vacancies, which are known to critically affect electron distribution, structural distortion, and overall functionality in perovskite oxides, remain insufficiently explored in the context of entropy-stabilized systems. In contrast to the aforementioned works, this study systematically investigates the role of oxygen vacancies as a tunable parameter in the high-entropy perovskite system L5BO3. By carefully regulating oxygen partial pressure during thin-film deposition, we directly control the vacancy concentration and explore its effect on the local structure and electrical transport properties. This approach not only provides a new understanding of defect-mediated behavior in high-entropy oxides but also introduces a novel pathway for functional property modulation through vacancy engineering—a direction not addressed in previous studies.

The $La(Cr_{0.2}Mn_{0.2}Fe_{0.2}Co_{0.2}Ni_{0.2})O_3$ thin film, as an ABO_3 perovskite transition-metal oxide, exhibits strong electron correlations and diverse functionalities. By doping with different cations, one can manipulate charge, orbital, and spin characteristics, thereby influencing macroscopic behaviors such as electrical and magnetic properties. Researches indicate that this material holds significant potential in structural and mechanistic studies, opening new avenues for exploration. Although extensive research has provided a

solid understanding of L5BO3's fundamental properties, the role of oxygen vacancies remains unclear. In conventional perovskite oxides, oxygen vacancy density often dictates electron distribution and functionalities. In this paper, by adjusting the proportion of oxygen vacancies in the entropy-stabilized perovskite system, L5BO3 thin films were grown on (001) $SrTiO_3$ (STO) substrates, and vacancy states and their effect on the structural and electrical properties were investigated.

II. MATERIAL AND METHODS

A. Thin film preparation

The L5BO3 PLD target was synthesized by standard solid-state reaction. High purity (>99.9%) La_2O_3, Cr_2O_3, NiO, Fe_2O_3, MnO_2, and Co_3O_4 powders were mixed according to the stoichiometric ratio with a ball milling machine for 8 h. The mixed powder was calcined at 1000 °C in air for 12 h. Upon pressing into a pellet, sintering of the pellet was performed at 1300 °C for 12 h. Prior to film deposition, (001) $SrTiO_3$ (STO) substrates were subjected to leaching and thermal treatment for atomically flat TiO_2-terminated surfaces: substrates were leached in distilled water and annealed in the air at 1250 °C for 2 h.[20] The L5BO3 thin films (thickness = 30 nm) were deposited on STO at a substrate temperature of 700 °C. Different oxygen partial pressures (P_{O_2} = 1, 10, 100, 200 mTorr) were used.

B. Thin film characterization

The L5BO3 films were characterized by an x-ray diffractometer (XRD, Rigaku SmartLab) for the crystallinity and atomic force microscopy (AFM, Bruker Multi-Mode 8) for the surface morphology. As the films were prepared under different P_{O_2}, elemental composition and valency of the constituents were estimated by x-ray photoelectron spectroscopy (XPS, Thermo Fisher ESCALAB XI+). The sample surface was cleaned by *in situ* ion milling before measurements to eliminate surface contamination. Binding energies in this work were calibrated with C 1s peaks (284.8 eV). The microstructure of the films was characterized with transmission electron microscopy (TEM). TEM specimens were prepared by using the focused ion-beam (FIB) technique. High-angle annular dark-field (HAADF) and integrated differential phase contrast (iDPC) images were acquired to identify locations of cations and oxygens. The energy-dispersive x-ray spectroscopy (EDS) was used to identify the distribution of elements.

To perform electrical measurements on the films, Ti/Au striped electrodes were patterned with stainless steel mechanical masks and deposited with electron-beam evaporation. Electrical measurements were performed with a physical property measurement system (PPMS, Quantum Design).

III. RESULTS

Figure 1(a) presents the XRD θ–2θ profiles around the (002) reflections of the 30 nm L5BO3/STO (001) thin films grown under oxygen pressures ranging from 1 to 200 mTorr. All scans clearly show the STO (002) substrate peaks and the L5BO3 film peaks. The dots represent the STO (002), while the rhomboids indicate the 2θ positions of L5BO3 (002) for films prepared under different P_{O2}. The film peaks exhibit a distinct shift toward smaller angles as the oxygen deposition pressure decreases, indicating an increase in the out-of-plane lattice parameter from 3.87 to 3.95 Å.

The literature reports a lattice parameter of 3.871 Å for bulk L5BO3,[19] while our L5BO3 film grown at 200 mTorr ($L5BO3_{200mTorr}$) shows a comparable out-of-plane lattice parameter of 3.87 Å, suggesting that it is close to the bulk material.

Laue oscillations that originate from the incomplete destructive interference of unit cells could be observed on the two sides of the

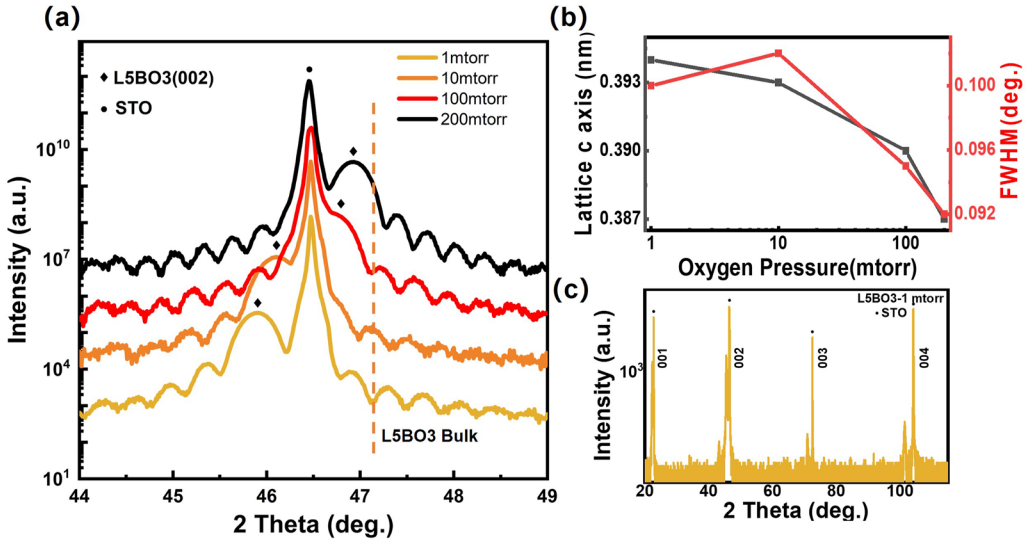

FIG. 1. X-ray patterns of L5BO3/STO films prepared under 1–200 mTorr O_2 partial pressures. (a) θ–2θ scan around the (002) reflections of L5BO3 and STO, with the dashed line indicating the lattice of bulk L5BO3. (b) The out-of-plane lattice parameter and FWHM of the L5BO3 films. (c) An overview scan of an L5BO3 thin film grown at 1 mTorr O_2 partial pressure ($L5BO3_{1mTorr}$).

film Bragg peak for all the films, suggesting good film crystallinity with low defect density.[19] A full-width at half-maximum (FWHM) value of 0.100 to 0.087 in the rocking curve for the films indicates a low mosaic spread of the film crystals [Fig. 1(b)]. The increasing trend of FWHM values [Fig. 1(b), right axis] suggests a slight degradation in film quality with decreasing oxygen pressure. It should be noted that even with the slight degradation, film grown under 1 mTorr oxygen partial pressure shows a FWHM value of 0.100, which supports the good film quality. The film was subjected to an overview scan [Fig. 1(c)]. Only diffraction peaks corresponding to (002) could be observed, indicating the film with a promising single phase with the absence of secondary phases and incomplete reaction from constituent elements.

In addition, with the decreasing oxygen pressure, the L5BO3 (002) peak shifts to lower angles; it may indicate the increased oxygen vacancy contents in the L5BO3. As all the films were grown on the same type of substrate, STO, and with the same deposition temperature, the strain induced by the substrate on the films is expected to be identical. The only modified parameter was oxygen deposition pressure. A trend of increasing oxygen vacancies would be expected for films prepared at lower oxygen deposition pressures, resulting in a reduction of the valence of the B site elements. With the fact that ions with lower valence states have larger ionic radii, the XRD peak would shift to a lower angle according to Bragg's rule. Our XRD measurements indicate well-identified single crystals for all the films made with various oxygen vacancies.

Figure 2 shows the TEM images of films grown in oxygen-rich [Figs. 2(a1) and 2(a2)] and deficient [Figs. 2(b1) and 2(b2)] environments. From the low magnification HAADF images in Figs. 2(a1) and 2(b1), both films show a sharp film–substrate interface. The inset shows the highly regular atomic periodic arrangement of both the A and B site atoms. The lattice constants of 100 and 1 mTorr

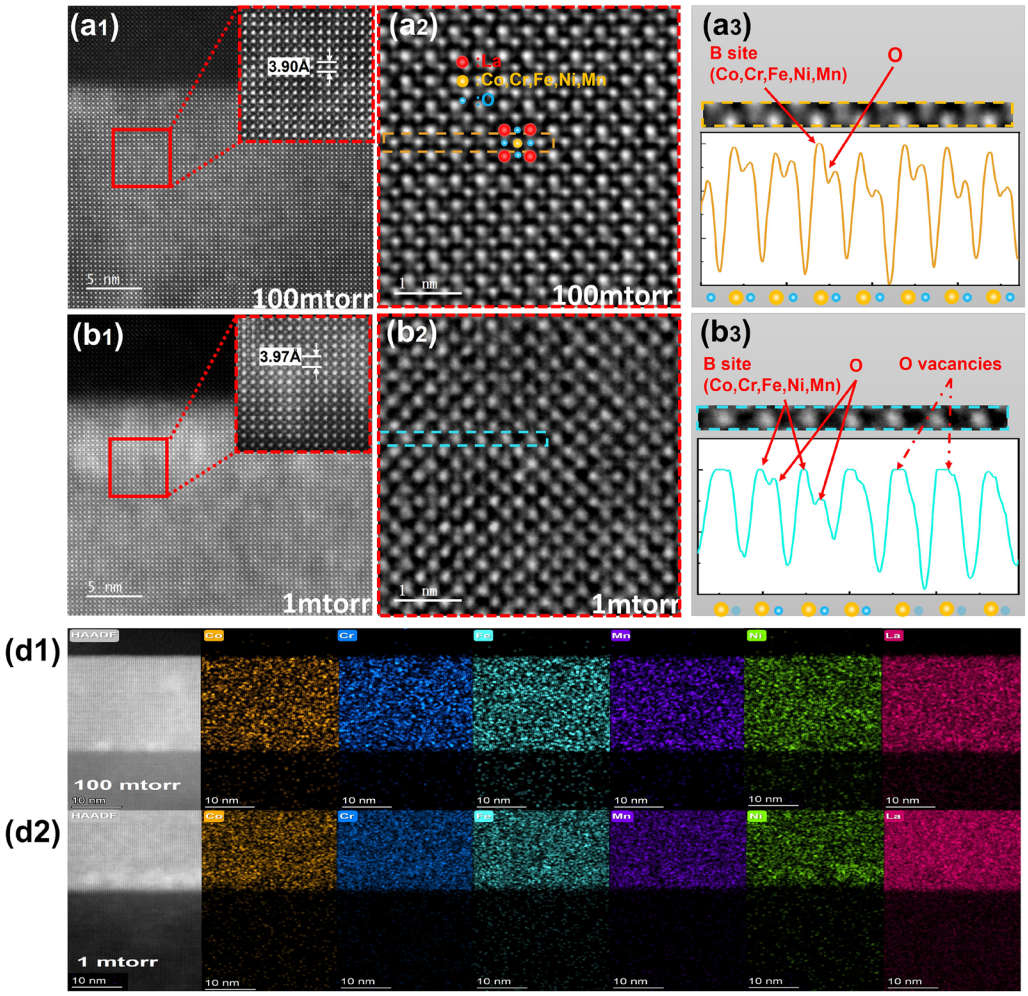

FIG. 2. Cross-sectional TEM images of $L5BO3_{100mTorr}$ and $L5BO3_{1mTorr}$ films: Panels (a1) and (b1) show the TEM images, while panels (a2) and (b2) show the iDPC images of selected areas. Line profiles in panels (a3) and (b3) display the average intensity of B-site atoms and oxygen (O) atoms over the regions highlighted by yellow and green dotted-line squares. The yellow and blue circles indicate the positions of B-site elements and oxygen atoms, respectively, while the transparent blue circles denote the oxygen vacancies. EDS images of 100 mTorr (d1) and 1 mTorr (d2) partial pressure grown L5BO3 films.

are around 3.90 and 3.97 Å, respectively, which are close to the data calculated by XRD [Fig. 1(b)]. Owing to the better atomic contrast of both heavy and light elements of the iDPC technique, oxygen atoms could be identified in the iDPC TEM images. Intensity profiles [Figs. 2(a3) and 2(b3)] were extracted from the selected area as highlighted in Figs. 2(a2) and 2(b2). The intensity profile from the $L5BO3_{100mTorr}$ clearly shows the oxygen atoms lying between B-site atoms [Fig. 2(a3)], while missing oxygen (forming oxygen vacancies) was found in $L5BO3_{1mTorr}$ [Fig. 2(b3)]. The oxygen at the selected area in Fig. 2(b2) has significant positional shifts compared to the $L5BO3_{100mTorr}$, as shown in Fig. 2(a2). The high peaks with their shoulders are the B-site elements and their neighbor oxygen atoms, as indicated by the solid arrows [Fig. 2(a3)]. In addition, the dotted arrows are pointed at the vanished shoulder peaks, which correspond to the oxygen vacancies. The oxygen vacancy concentrations are compared based on the absence of peaks at O-sites, which are presented as lighter blue circles in the B site-O sequences. It is confirmed that the concentration of oxygen vacancy in the $L5BO3_{1mTorr}$ is higher than that in the $L5BO3_{100mTorr}$. EDS mappings of the $L5BO3_{100mTorr}$ [Fig. 2(d1)] and $L5BO3_{1mTorr}$ [Fig. 2(d2)] demonstrate homogeneous distributions of La, Co, Cr, Fe, Mn, and Ni elements.

Figure 3(a) presents the temperature (T)-dependent resistivity (ρ) curves of L5BO3/STO thin films grown under different oxygen pressures. All the films exhibit typical semiconductor behavior, with the resistivity decreases as the temperature rises from 150 to 400 K. Figure 3(a) also shows that the resistivity of the films increases with decreasing oxygen partial pressure (P_{O_2}), which correlates with an increase in oxygen vacancy concentration.

The resistivity ρ of the samples depends on T and the activation energy (E_a), as described by the following equation:

$$\rho = \frac{T}{\rho_0 e^{E_a/(k_B T)}}, \tag{3}$$

where k_B is the Boltzmann constant, ρ_0 is the pre-exponential factor (dependent on the material's intrinsic properties but independent of temperature), and E_a can be calculated from the slope of the linear fitting curves in Fig. 4(b). As the oxygen deposition pressure decreases, E_a increases from 240 to 310 meV. This is attributed to oxygen vacancies, which act as hole dopants, reducing the Fermi level and enhancing the activation energy with increasing oxygen vacancy concentration.[21]

Two conduction mechanisms, small polaron hopping (SPH) and Mott's variable range hopping (Mott-VRH), are commonly used to explain electrical conduction in insulating materials.[22] The SPH conduction is described by Eq. (4)

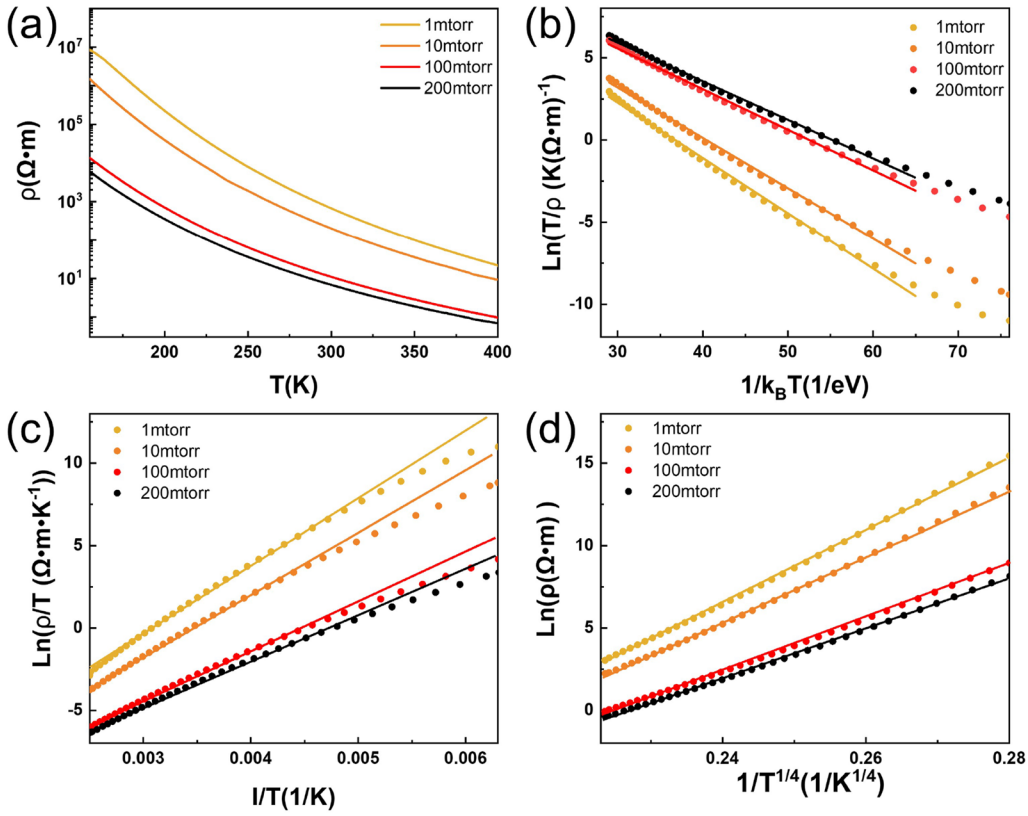

FIG. 3. (a) Temperature-dependent resistivity curves of L5BO3 films grown under different oxygen partial pressures. (b) Plot of $\ln(T/\rho)$ as a function of $1/(k_B T)$. (c) Plot of $\ln(\rho/T)$ as a function of $1/T$. (d) Plot of $\ln(\rho)$ as a function of $T^{-1/4}$. The lines in panels (b)–(d) represent the linear fitting curves based on Eqs. (3)–(5), respectively.

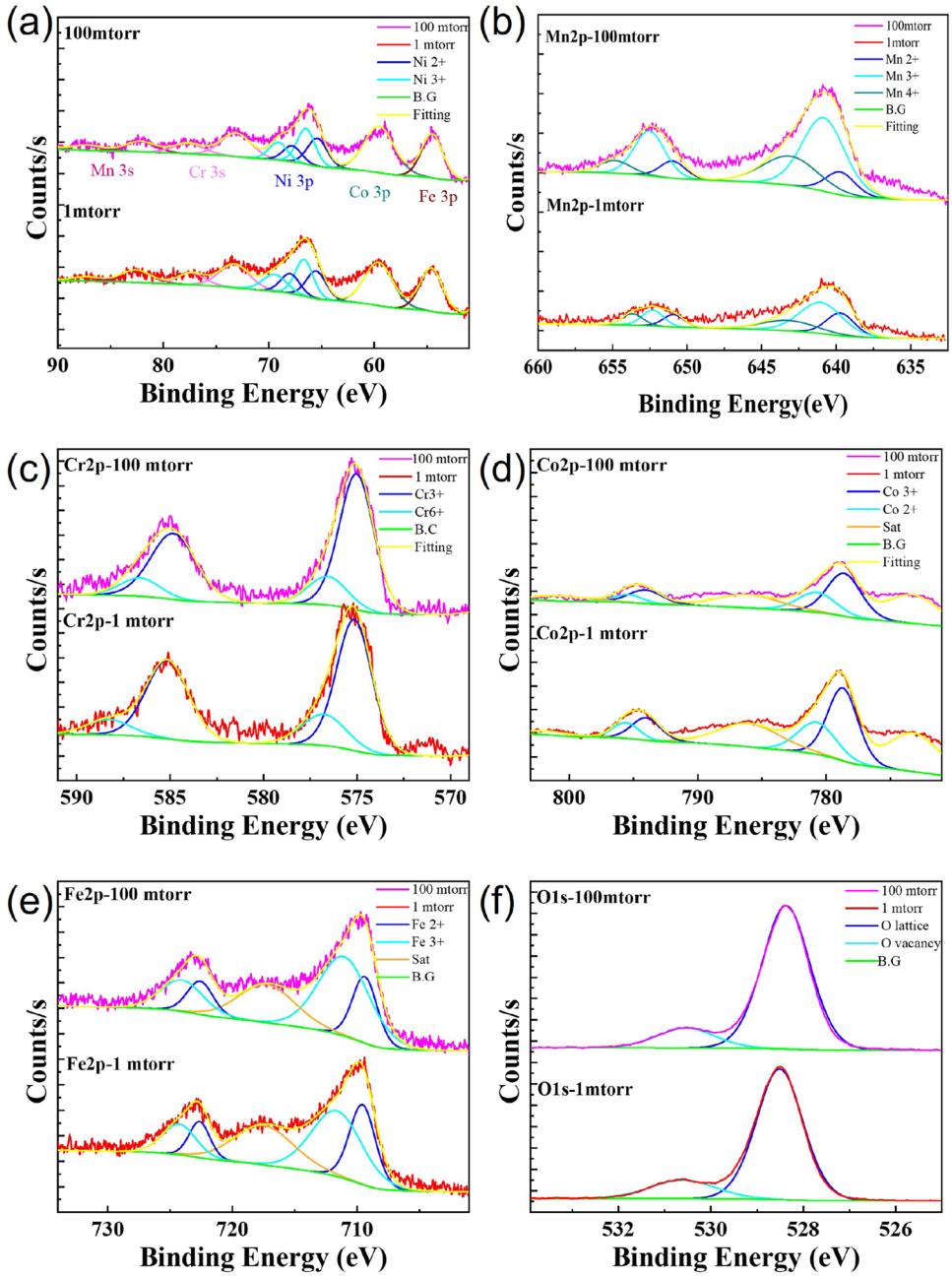

FIG. 4. (a) XPS spectra with binding energy ranging from 90 to 50 eV to show Ni 3p, Co 3p, Fe 3p, Cr 3s, and Mn 3s peaks of 100 and 1 mTorr samples. XPS spectra for the Mn 2p (b), Cr 2p (c), Co 2p (d), Fe 2p (e), and O 1s (f) of the $L5BO3_{100mTorr}$ and $L5BO3_{1mTorr}$. [Fitting by advantage, FWHM variation ≤0.2 eV for the same oxidation state, calibrated using C 1s (284.8 eV)].

$$\rho = \rho_\alpha T e^{E_a/(k_B T)}, \tag{4}$$

where $\rho_\alpha = \left[\frac{k_B}{\nu_{ph} N e^2 R^2 C(1-C)}\right] e^{2\alpha R}$. Here, N is the number of ion sites per unit volume, $R = (1/N)^{1/3}$ is the average intersite spacing, C is the fraction of sites occupied by a polaron, α is the electron wave function decay constant, and ν_{ph} is the optical phonon frequency (estimated as $h\nu_{ph} = k_B\theta_D$, where θ_D is the Debye temperature).[23]

SPH describes the thermally activated hopping of electrons (polarons) between lattice sites in systems with strong electron–phonon coupling and local lattice distortions. The activation energy E_a represents the energy required for polarons to overcome local barriers, leading to an increase in conductivity with rising temperature, following an exponential relationship. When the concentration of oxygen vacancies increases, the resistivity of the oxide also increases.[24]

The common Mott-VRH expression is Eq. (5),

$$\rho = \rho_0 e^{\left(\frac{T_0}{T}\right)^{\frac{1}{4}}}. \quad (5)$$

ρ_0 is a pre-exponential parameter, and T_0 is a parameter that depends on the state density at the Fermi level. Compared to the SPH, the Mott-VRH usually exists in the disordering system and provides an energy-efficient method to transport electrons. At low temperatures, electrons thermally excite localized states that are lower in energy but spatially distant, thereby enabling electrical conduction. This process relies on the density and distribution of localized states within the material.[25,26]

From the measured resistivity of the L5BO3/STO thin films at room temperature, they present the Mott-VRH conduction mechanisms. By plotting $\ln(\rho/T)$ as a function of T^{-1} [Fig. 3(c)] and $\ln(\rho)$ as a function of $1/T^{1/4}$ [Fig. 3(d)], a certain linear relationship of the curves can be observed in Fig. 3(d), which corresponds to the Mott-VRH conduction mechanism for L5BO3.

However, based on the trend of resistivity changes with growth oxygen pressure, it should ideally align more with the SPH model. However, data analysis shows that the relationship between temperature and resistivity better fits the Mott-VRH model.

Oxygen vacancies introduce localized states into the bandgap of the material. These localized states can serve as hopping sites for electrons, thereby affecting the effectiveness and frequency of the hopping process, which means reducing resistivity. Consequently, as the concentration of oxygen vacancies increases, resistivity decreases.

Conventionally, according to the Mott-VRH model, an increase in oxygen vacancies is expected to introduce additional free carriers and defect states, thereby enhancing carrier hopping and reducing resistivity. However, in our L5BO3 thin films, an increase in oxygen vacancy concentration is accompanied by a rise in resistivity. The multi-valence of transition metal and high-spin-state ions may inhibit the conductivity of Mott-VRH materials through mechanisms such as spin-related scattering. These effects make the electron hopping process more difficult, thereby increasing the material's resistivity. This anomalous behavior can be attributed to the complex interplay between oxygen vacancies and the valence state evolution of the five B-site cations (Cr, Mn, Fe, Co, Ni) in the high-entropy perovskite structure. XPS analysis (Fig. 4) confirms that with increasing oxygen deficiency, significant changes occur in the oxidation states of these transition metals, leading to the formation of higher-spin-state ions (e.g., from high-spin Co^{3+} to low-spin Co^{2+}, Fe^{3+} to Fe^{2+}, etc.),[27] reducing the effective density of localized states,[28] and increasing activation energy.[29]

High-spin ions introduce magnetic disorder, increasing spin–flip scattering events and thereby suppressing coherent electron hopping.[30] In addition, according to Mott's law,[31]

$$\rho(T) = \rho_0 \exp\left(\left(\frac{T_0}{T}\right)^{1/4}\right), \quad \text{where } T_0 \propto \frac{1}{N(E_F)\xi^3}. \quad (6)$$

The hopping activation energy T_0 is inversely proportional to $N(E_F)$ and the localization length ξ; a decrease in $N(E_F)$ or shrinkage of ξ due to enhanced electron–lattice interactions can substantially raise T_0, leading to higher resistivity.[32] Thus, even though oxygen vacancies nominally supply more carriers, the concomitant valence and spin state transitions dominate the electronic transport by reducing $N(E_F)$ and increasing scattering, ultimately overriding the vacancy-induced conductivity enhancement and resulting in a net increase in resistivity.

Therefore, we used XPS to detect the valence change of L5BO3 films grown at 1, 10, and 100 mTorr oxygen partial pressures, identifying high-spin-state ions. Table I summarizes the elemental composition, electronic structure, and valence changes of B-site elements, as well as the lattice oxygen (O_l) to oxygen vacancy (O_v) ratio. The surface elemental distribution, particularly for Mn, Cr, Ni, Co, Fe, and O, is shown for films grown at 1, 10, and 100 mTorr. Figure 4 compares the XPS spectra for films grown at 1 and 100 mTorr.

Figure 4(a) shows the binding energy range from 90 to 50 eV, which includes Mn 3s, Cr 3s, Ni 3p, Co 3p, and Fe 3p XPS peaks. The peak splitting (ΔE) is significant evidence for identifying the Mn oxidation state. According to Fig. 4(a), the ΔE values are 4.53 and 4.69 eV for $L5BO3_{100mTorr}$ and $L5BO3_{1mTorr}$, respectively. These values, between 4.5 and 5.3 eV, indicate that Mn valence states lie between 3+ and 4+.[33]

Figure 4(b) details the distribution of Mn^{4+} (643.2 eV), Mn^{3+} (641.0 eV), and Mn^{2+} (639.8 eV).[33] In the $L5BO3_{100mTorr}$ sample, the ratio of Mn^{4+}:Mn^{3+}:Mn^{2+} is 29.6%:57.9%:12.5%, while for $L5BO3_{1mTorr}$, Mn^{2+} increases to 25.5%, and Mn^{3+} and Mn^{4+} decrease to 52.1% and 22.4%, respectively. These results suggest that increasing oxygen vacancies induces multivalent Mn states (Mn^{4+}, Mn^{3+}, and Mn^{2+}) due to electron transfer through O 2p orbitals to Mn outer orbitals.

TABLE I. Data of distribution of multi-valence of Mn, Cr, Co, Fe, Ni, and O ions; ω is the changing value of the B^{3+} between 1 and 100 mTorr.

		Oxygen partial pressure for film growth			
Element	Valence ratio	100 mTorr	10 mTorr	1 mTorr	ω%
Mn	Mn^{4+}:Mn^{3+}:Mn^{2+}	29.6%:57.9%:12.5%	24.6%:55.9%:19.5%	22.4%:52.1%:25.5%	−14.7
Cr	Cr^{3+}:Cr^{6+}	80.8%:19.2%	76.9%:23.1%	68.5%:31.5%	−12.3
Co	Co^{3+}:Co^{2+}	61.3%:38.7%	65.7%:34.3%	67.1%:32.9%	5.8
Fe	Fe^{3+}:Fe^{2+}	71.1%:28.9%	61.6%:30.4%	45.4%:54.6%	−25.7
Ni	Ni^{3+}:Ni^{2+}	53.9%:46.1%	54.8%:45.2%	61.2%:38.8%	7.3
O	O_l:O_v	79.4%:20.6%	78.1%:21.9%	76.3%:23.7%	

The Cr 3s spectrum [Fig. 4(a)] shows peaks at 73.31 and 77.38 eV for $L5BO3_{1mTorr}$, with $\Delta E = 4.07$ eV, and at 73.12 and 77.62 eV for $L5BO3_{100mTorr}$, with $\Delta E = 4.5$ eV.[34] The smaller ΔE in $L5BO3_{1mTorr}$ indicates charge transfer from Cr to other elements, reducing the overlap of Cr 3s and 3d orbitals. Figure 4(c) highlights the Cr^{3+} and Cr^{6+} proportions. As oxygen pressure decreases, the Cr^{3+} ratio drops from 80.8% to 68.5%, indicating enhanced charge transfer to Cr^{6+}. Cr^{6+} introduces high-energy empty orbitals that act as trapping centers for electrons or holes, significantly influencing carrier mobility and increasing resistance.[35]

Figure 4(d) shows Co^{2+}, Co^{3+}, and two shake-up satellites fitted via the Co 2p spectrum, with peaks at 778.6 eV (Co^{2+}) and 780.7 eV (Co^{3+}).[36,37] Figure 4(e) shows the Fe 2p spectrum, with Fe^{2+} at 709.6 eV and Fe^{3+} at 711.6 eV.[35] In $L5BO3_{100mTorr}$, the Co^{3+} ratio is 61.3%, lower than the 67.1% in $L5BO3_{1mTorr}$, whereas the Fe^{3+} ratio is 71.1%, higher than the 45.4% in $L5BO3_{1mTorr}$. This indicates electron transfer from Co orbitals to Fe orbitals as oxygen vacancies increase.

Due to the overlap of Ni 2p peaks with La 3d, Ni 3p peaks were analyzed instead. The blue curves in Fig. 4(a) show Ni^{3+} and Ni^{2+} fitting spectra at 68.3 and 67.6 eV, respectively.[38] The Ni^{3+} proportion increases from 53.92% in $L5BO3_{100mTorr}$ to 61.2% in $L5BO3_{1mTorr}$, suggesting electron transfer from Ni 3d orbitals to other elements in a low-oxygen environment. However, Co^{2+} ($3d^7$), Fe^{2+} ($3d^6$), and Ni^{2+} ($3d^8$) in their high-spin states induce local magnetic variations that increase resistance.[39] Although the Co^{2+} and Ni^{2+} content decreases in 1 mTorr, the increase in Fe^{2+}, Cr^{6+}, and Mn^{2+} outweighs this, resulting in overall increased resistance.

In summary, in the $L5BO3_{1mTorr}$, electrons transfer from Cr, Co, and Ni to Fe and Mn via O 2p orbits, as compared to the $L5BO3_{100mTorr}$. This valence change indicates oxygen vacancies in the L5BO3 thin film. Figure 4(f) shows that the $L5BO3_{1mTorr}$ has 23.7% O vacancy and 76.3% O lattice, compared to 20.6% O vacancy and 79.4% O lattice in the $L5BO3_{100mTorr}$, confirming more oxygen vacancies in the $L5BO3_{1mTorr}$.[40] With the decreasing oxygen pressure, the L5BO3 thin film will form more oxygen vacancies. From an overall macroscopic perspective, the oxygen vacancy makes the B site elements move to lower valence and higher spin–orbit. Through the effect of the Mott-VRH mode, a higher spin state of B-site elements can also cause an increase in resistivity. In the same period, ions with a lower valence states have larger radii, and according to Bragg's formula, the lattice peak shifts to a lower angle, which is shown in Fig. 1(a).

IV. CONCLUSION

In this work, we successfully fabricated $La(Cr_{0.2}Mn_{0.2}Fe_{0.2}Co_{0.2}Ni_{0.2})O_3$ single-crystal thin films on STO (001) substrates with varying oxygen vacancy densities. The samples demonstrated excellent crystallinity, surface electronic structure, short-range order, and uniform B-site element distribution, as confirmed by XRD, XPS, and TEM analyses.

Our study reveals that the increased oxygen vacancy concentration and the charge transfer pathways between transition metals are key factors governing the significant rise in the resistivity of L5BO3 and its electron conduction mechanism (Mott-VRH). The multi-valence states of B-site elements disrupt electron localization in L5BO3 thin films, impeding electron transport and further validating the material's adherence to the Mott-VRH mechanism. This work provides insights into defect engineering and electronic behavior in complex oxides. These findings pave the way for optimizing the performance of high-entropy perovskites in functional applications, such as resistive switching devices, thermoelectrics, and energy-efficient semiconductors. Such advancements could unlock new opportunities for next-generation electronic and energy materials.

ACKNOWLEDGMENTS

The work is supported by the Research Grants Council, HKSAR (Grant No. 15302222), the Hong Kong Polytechnic University (WZA1), the Natural Science Foundation of China (Grant Nos. 52173226, 52130108, and 42173029), and the Pear River Talent program from the Department of Science and Technology of Guangdong Province (Grant No. 2021CX02C).

AUTHOR DECLARATIONS

Conflict of Interest

The authors have no conflicts to disclose.

Author Contributions

Xin Yuan: Data curation (lead); Formal analysis (lead); Investigation (lead); Writing – original draft (lead); Writing – review & editing (lead). **Sheung Mei Ng**: Data curation (equal); Formal analysis (equal); Investigation (equal); Writing – review & editing (equal). **PeiGen Li**: Data curation (equal); Writing – review & editing (equal). **JingMing Liang**: Data curation (equal); Investigation (equal). **Hon Fai Wong**: Resources (equal); Software (equal). **ChuangShi Feng**: Data curation (equal); Resources (equal). **Shuai Nan**: Investigation (equal); Resources (equal). **HongQuan Song**: Formal analysis (equal); Methodology (equal). **Zhou Guan**: Data curation (equal); Resources (equal). **FuXiang Zhang**: Data curation (equal); Resources (equal); Software (equal); Writing – review & editing (equal). **Chi Wah Leung**: Resources (equal); Supervision (equal); Writing – review & editing (equal).

DATA AVAILABILITY

The data that support the findings of this study are available from the corresponding author upon reasonable request.

REFERENCES

[1] J. M. Rondinelli, S. J. May, and J. W. Freeland, "Control of octahedral connectivity in perovskite oxide heterostructures: An emerging route to multifunctional materials discovery," MRS Bull. **37**, 261–270 (2012).

[2] H. Wei, C. Yang, Y. Wu, B. Cao, M. Lorenz, and M. Grundmann, "From energy harvesting to topologically insulating behavior: ABO_3-type epitaxial thin films and superlattices," J. Mater. Chem. C **8**, 15575–15596 (2020).

[3] L. Xu, Z. Wang, B. Su, C. Wang, X. Yang, R. Su, X. Long, and C. He, "Origin of structural change driven by a-site lanthanide doping in ABO_3-type perovskite ferroelectrics," Crystals **10**, 434 (2020).

[4] J. A. Grovogui, T. J. Slade, S. Hao, C. Wolverton, M. G. Kanatzidis, and V. P. Dravid, "Implications of doping on microstructure, processing, and thermoelectric performance: The case of PbSe," J. Mater. Res. **36**, 1272–1284 (2021).

[5]J. P. Attfield, A. L. Kharlanov, and J. A. McAllister, "Cation effects in doped La_2CuO_4 superconductors," Nature **394**, 157–159 (1998).
[6]C. W. Rischau, X. Lin, C. P. Grams, D. Finck, S. Harms, J. Engelmayer, T. Lorenz, Y. Gallais, B. Fauqué, J. Hemberger, and K. Behnia, "A ferroelectric quantum phase transition inside the superconducting dome of $Sr_{1-x}Ca_xTiO_{3-\delta}$," Nat. Phys. **13**, 643–648 (2017).
[7]H. J. Zhao, X. Q. Liu, X. M. Chen, and L. Bellaiche, "Effects of chemical and hydrostatic pressures on structural, magnetic, and electronic properties of R_2NiMnO_6 (R = rare-earth ion) double perovskites," Phys. Rev. B **90**, 195147 (2014).
[8]J. Cheng, A. Navrotsky, X.-D. Zhou, and H. U. Anderson, "Enthalpies of formation of $LaMO_3$ perovskites (M = Cr, Fe, Co, and Ni)," J. Mater. Res. **20**, 191–200 (2005).
[9]C. M. Rost, E. Sachet, T. Borman, A. Moballegh, E. C. Dickey, D. Hou, J. L. Jones, S. Curtarolo, and J.-P. Maria, "Entropy-stabilized oxides," Nat. Commun. **6**, 8485 (2015).
[10]A. Sarkar, R. Djenadic, D. Wang, C. Hein, R. Kautenburger, O. Clemens, and H. Hahn, "Rare earth and transition metal based entropy stabilised perovskite type oxides," J. Eur. Ceram. Soc. **38**, 2318–2327 (2018).
[11]A. Sarkar, Q. Wang, A. Schiele, M. R. Chellali, S. S. Bhattacharya, D. Wang, T. Brezesinski, H. Hahn, L. Velasco, and B. Breitung, "High-entropy oxides: Fundamental aspects and electrochemical properties," Adv. Mater. **31**, 1806236 (2019).
[12]Z. Meng, X. Gong, J. Xu, X. Sun, F. Zeng, Z. Du, Z. Hao, W. Shi, S. Yu, X. Hu, and H. Tian, "A general strategy for preparing hollow spherical multilayer structures of oxygen-rich vacancy transition metal oxides, especially high entropy perovskite oxides," Chem. Eng. J. **457**, 141242 (2023).
[13]S. Jiang, T. Hu, J. Gild, N. Zhou, J. Nie, M. Qin, T. Harrington, K. Vecchio, and J. Luo, "A new class of high-entropy perovskite oxides," Scr. Mater. **142**, 116–120 (2018).
[14]W. Xiao, Y. Li, A. Elgendy, E. C. Duran, M. A. Buckingham, B. F. Spencer, B. Han, F. Alam, X. Zhong, S. H. Cartmell *et al.*, "Synthesis of high entropy and entropy-stabilized metal sulfides and their evaluation as hydrogen evolution electrocatalysts," Chem. Mater. **35**, 7904–7914 (2023).
[15]W. Yin, X. Nie, X. Shi, J. Wang, and Z. Sun, "S-vacancy-rich iron sulfide derived from high-entropy Prussian blue for enhanced sodium-ion storage," J. Power Sources **629**, 236021 (2025).
[16]N. Zhang, Z. Xing, Z. Li, and W. Zhou, "Sulfur vacancy engineering of metal sulfide photocatalysts for solar energy conversion," Chem Catal. **3**, 100375 (2023).
[17]Y. Sharma, Q. Zheng, A. R. Mazza, E. Skoropata, T. Heitmann, Z. Gai, B. Musico, P. F. Miceli, B. C. Sales, V. Keppens *et al.*, "Magnetic anisotropy in single-crystal high-entropy perovskite oxide La $(Cr_{0.2}Mn_{0.2}Fe_{0.2}Co_{0.2}Ni_{0.2})O_3$ films," Phys. Rev. Mater. **4**, 014404 (2020).
[18]M. Brahlek, A. R. Mazza, K. C. Pitike, E. Skoropata, J. Lapano, G. Eres, V. R. Cooper, and T. Z. Ward, "Unexpected crystalline homogeneity from the disordered bond network in La $(Cr_{0.2}Mn_{0.2}Fe_{0.2}Co_{0.2}Ni_{0.2})O_3$ films," Phys. Rev. Mater. **4**, 054407 (2020).
[19]M. V. Kante, M. L. Weber, S. Ni, I. C. G. van den Bosch, E. van der Minne, L. Heymann, L. J. Falling, N. Gauquelin, M. Tsvetanova, D. M. Cunha *et al.*, "A high-entropy oxide as high-activity electrocatalyst for water oxidation," ACS Nano **17**, 5329–5339 (2023).
[20]J. G. Connell, B. J. Isaac, G. B. Ekanayake, D. R. Strachan, and S. S. A. Seo, "Preparation of atomically flat $SrTiO_3$ surfaces using a deionized-water leaching and thermal annealing procedure," Appl. Phys. Lett. **101**, 251607 (2012).
[21]G. R. Stewart, "Non-fermi-liquid behavior in *d*-and *f*-electron metals," Rev. Mod. Phys. **73**, 797 (2001).
[22]M. Gurvitch, "Ioffe–Regel criterion and resistivity of metals," Phys. Rev. B **24**, 7404 (1981).
[23]N. Panwar, D. K. Pandya, A. Rao, K. K. Wu, N. Kaurav, Y. K. Kuo, and S. K. Agarwal, "Electrical and thermal properties of $Pr_{2/3}(Ba_{1-x}Cs_x)_{1/3}MnO_3$ manganites," Eur. Phys. J. B **65**, 179–186 (2008).
[24]M. Reticcioli, U. Diebold, G. Kresse, and C. Franchini, "Small polarons in transition metal oxides," in *Handbook of Materials Modeling: Applications: Current and Emerging Materials* (Springer Nature Switzerland AG, 2020), pp. 1035–1073.
[25]B. I. Shklovskii and A. L. Efros, "Variable-range hopping conduction," Springer Ser. Solid-State Sci. **45**, 202–227 (1984).
[26]D. Yu, C. Wang, B. L. Wehrenberg, and P. Guyot-Sionnest, "Variable range hopping conduction in semiconductor nanocrystal solids," Phys. Rev. Lett. **92**, 216802 (2004).
[27]D. J. Groenendijk, C. Autieri, J. Girovsky, M. C. Martinez-Velarte, N. Manca, G. Mattoni, A. M. R. V. L. Monteiro, N. Gauquelin, J. Verbeeck, A. Otte *et al.*, "Spin-orbit semimetal $SrIrO_3$ in the two-dimensional limit," Phys. Rev. Lett. **119**, 256403 (2017).
[28]M. Foygel and A. G. Petukhov, "Variable-range hopping of spin and lattice polarons: Coulomb correlation effects," Phys. Rev. B **70**, 224212 (2004).
[29]R. Schmidt, A. Basu, and A. W. Brinkman, "Small polaron hopping in spinel manganates," Phys. Rev. B **72**, 115101 (2005).
[30]A. Gupta and J. Z. Sun, "Spin-polarized transport and magnetoresistance in magnetic oxides," J. Magn. Magn. Mater. **200**, 24–43 (1999).
[31]Y. Tokura and N. Nagaosa, "Orbital physics in transition-metal oxides," Science **288**, 462–468 (2000).
[32]M. Imada, A. Fujimori, and Y. Tokura, "Metal-insulator transitions," Rev. Mod. Phys. **70**, 1039 (1998).
[33]M. Fujiwara, T. Matsushita, and S. Ikeda, "Evaluation of $Mn3_S$ x-ray photoelectron spectroscopy for characterization of manganese complexes," J. Electron Spectrosc. Relat. Phenom. **74**, 201–206 (1995).
[34]V. Tsurkan, M. Demeter, B. Schneider, D. Hartmann, and M. Neumann, "Exchange splitting of the Cr, Fe and Mn 3s XPS spectra in some ternary magnetic semiconductor sulphides," Solid State Commun. **114**, 149–154 (2000).
[35]K. P. Thiruppathi and D. Nataraj, "Precisely tailored $LaFeO_3$ dendrites using urea and piperazine hexahydrate for the highly selective and sensitive detection of trace level acetone," Mater. Adv. **1**, 2971–2982 (2020).
[36]X. Chen, Q. Wang, Z. Cheng, M. Zhu, H. Zhou, P. Jiang, L. Zhou, Q. Xue, F. Yuan, J. Zhu *et al.*, "Direct observation of chemical short-range order in a medium-entropy alloy," Nature **592**, 712–716 (2021).
[37]V. S. Marakatti, M. Ronda-Lloret, M. Krajčí, B. Joseph, C. Marini, J. J. Delgado, F. Devred, N. R. Shiju, and E. M. Gaigneaux, "Highly active and stable Co (Co_3O_4)_Sm_2O_3 nano-crystallites derived from Sm_2Co_7 and $SmCo_5$ intermetallic compounds in NH_3 synthesis and CO_2 conversion," Catal. Sci. Technol. **12**, 686–706 (2022).
[38]A. N. Mansour and C. A. Melendres, "Characterization of electrochemically prepared *γ*-NiOOH by XPS," Surf. Sci. Spectra **3**, 271–278 (1994).
[39]K. Gaur, S. C. Verma, and H. B. Lal, "Defects and electrical conduction in mixed lanthanum transition metal oxides," J. Mater. Sci. **23**, 1725–1728 (1988).
[40]J. S. Yoon, Y.-S. Lim, B. H. Choi, and H. J. Hwang, "Catalytic activity of perovskite-type doped $La_{0.08}Sr_{0.92}Ti_{1-x}M_xO_{3-\delta}$ (M = Mn, Fe, and Co) oxides for methane oxidation," Int. J. Hydrogen Energy **39**, 7955–7962 (2014).